A New Neural Network Retrieval of Liquid Water Path Optimized for Mixed-Phase Cold Air Outbreaks Using Radiometer and Radar Observations

Samuel Ephraim* and Paquita Zuidema

Rosenstiel School Department of Atmospheric Sciences, University of Miami, Coral Gables, FL

Timothy W. Juliano

U.S. NSF National Center for Atmospheric Research, Boulder, CO

Coltin Grasmick, Bart Geerts and Jeff French

Department of Atmospheric Science, University of Wyoming, Laramie, WY

Maria Cadeddu

Argone National Laboratory, Batavia, IL

Andrew Pazmany

Prosensing, Inc., Amherst, MA

Sarah Woods

U.S. NSF National Center for Atmospheric Research, Boulder, CO

ABSTRACT

Cold-air outbreaks over high latitude oceans typically include mixed-phase clouds and precipitation, in particular liquid clouds that support snow and graupel through ice growth processes. The partitioning of the total water into the liquid and ice phases impacts both weather and climate prediction, but accurate measurements on the phase partitioning remain difficult to acquire, especially near-real-time. Here we present a neural network approach to retrieve liquid water path (LWP) using passive microwave measurements combined with vertically-integrated radar reflectivities. The approach is an extension of Cadeddu et al. (2009), with the novel addition of radar reflectivity. The neural network is trained using the Passive and Active Microwave radiative TRAnsfer (PAMTRA) code applied to output from numerical simulations of three independent cold-air outbreaks sampled during the Cold-Air Outbreaks in the Marine Boundary Layer Experiment (COMBLE) campaign. Brightness temperatures corresponding to the four sidebands of an upward-looking G-band (183 GHz) Vapor Radiometer, along with the vertically-integrated reflectivity from a zenith-pointing 95 GHz Wyoming Cloud Radar, are simulated from the perspective of a near-surface aircraft track. The radar reflectivity helps discriminate the snow contribution to the brightness temperatures. The neural network regression is thereafter tested on a simulation of an independent cold-air outbreak during COMBLE, and against measurements from the US Department of Energy Atmospheric Radiation Measurement North Slope of Alaska observatory. This neural network approach is shown to provide robust, computationally-efficient, near-real-time measurements of LWP and water vapor path during the Cold Air Outbreak Experiment in the Sub-Arctic Region (CAESAR) campaign in February-April 2024.

Significance statement. Heavy precipitation from mixed-phase clouds over the high-latitude open waters impacts shipping, fishing and coastal communities. Mixed-phase clouds are also a modeling challenge, inhibiting weather and climate prediction skill. More comprehensive measurements of the cloud liquid and ice occupying the same vertical column improve our understanding and ability to represent this challenging cloud type. Here we propose a new retrieval to distinguish the liquid water path within air columns that also contain ice.

1. Introduction

Cold-air outbreak (CAO) clouds in the Arctic are commonly mixed-phase (MP); however, the partitioning of the amount of ice and water in CAO clouds and precipitation is not always well observed. The process understanding of how cloud phases partition as a function of cloud lifecycle is important for the prediction of snowfall rates, convective

*Corresponding author: Samuel Ephraim, samuel.ephraim@earth.miami.edu

lifecycle, and intensity at weather timescales. The partitioning into liquid versus ice also has radiative impacts that are consequential for climate (Bodas-Salcedo et al. 2016a), with quiescent, liquid-containing, higher-albedo MP clouds able to possess a long lifetime despite being microphysically unstable (Zuidema et al. 2005b; Morrison et al. 2012), and warming the surface more effectively than ice clouds through longwave radiation (Korolev et al. 2017). Currently, overactive secondary ice production processes in global models deplete liquid in high-latitude clouds too readily (Bodas-Salcedo et al. 2016b) while simultaneously predicting too few ice-nucleating particles (McCluskey et al. 2023).

A better understanding of the relevant microphysical processes in Arctic MP CAOs requires accurate and representative measurements of the liquid water path (LWP), as part of a larger suite of measurements of microphysics, kinematics, and thermodynamics. Perhaps surprisingly, such measurements are not readily available. Spaced-based microwave satellite retrievals are stymied by large footprints that average over cloud inhomogeneities (Bremen et al. 2002) and can include surface contributions from sea ice (Zuidema and Joyce 2008), while retrievals based on visible imagery are uncertain because of solar zenith biases and three-dimensional radiative transfer effects (Khanal et al. 2020). Surface-based remote sensing assessments provide finer horizontal detail (Mages et al. 2023; Lackner et al. 2024) but may not capture the cloud evolution as comprehensively as an aircraft characterization (Abel et al. 2017; Seethala et al. 2024). *In-situ* measurements of total and liquid water content are useful but typically confined to spatial scales of ∼100 m (Korolev et al. 1998).

Within this suite of measurement strategies, airborne passive microwave measurements provide another path forward (McGrath and Hewison 2001). A recent spate of field campaigns has focused on high-latitude CAOs, both over the Southern Ocean, and north of Scandinavia, including the US Department of Energy (DOE) Cold-Air Outbreaks in the Marine Boundary Layer Experiment (COMBLE) Mobile Facility deployment in Andenes, Norway (Geerts et al. 2022). The US National Science Foundation further supported the Cold Air outbreak Experiment in the Sub-Arctic Region (CAESAR) aircraft campaign, based out of Kiruna, Sweden in spring of 2024, aboard the NSF NCAR C-130. A particular strength of the CAESAR campaign is a strong synergistic instrument suite of both *in-situ* and remote sensors. Within the CAESAR instrumentation suite, we focus on an upward-pointing G-band Vapor Radiometer (GVR), a passive microwave radiometer using frequencies near the 183.3 GHz water vapor absorption band, and a 95 GHz Wyoming Cloud Radar (WCR).

The GVR measurements are optimal for dry atmospheres, where the sensitivity to small changes in vapor and liquid is high. Surface-based passive microwave measurements near 183 GHz have been applied to Arctic MP clouds over Alaska (Cadeddu et al. 2009), and from aircraft to subtropical marine clouds (Zuidema et al. 2012). When further extended to convective Arctic MP clouds, the potential presence of snow, at sizes capable of scattering microwave radiation emitted from the surface back downwards towards the GVR, is an additional challenge. This motivates the use of vertically-integrated 95 GHz (W-band) radar reflectivities for identifying the larger ice particles.

To design the machine learning retrieval, the Passive and Active Microwave radiative TRAnsfer (PAMTRA) model (Mech et al. 2020) is applied to model representations of CAO clouds sampled during the COMBLE campaign period (Juliano et al. 2024). Limited-area-model (LAM) simulations use 1 km horizontal grid cell spacing, while a large-eddy-scale (LES) simulation is performed at 150 m horizontal grid cell spacing (dx). These simulations constitute the training and test datasets, respectively. Both sets of simulations use similar microphysical schemes. During CAESAR, we were able to validate the retrieved LWPs and WVPs with data from the *in-situ* microphysical probes. Additional testing uses GVR and Ka-band ARM Zenith Radar (KAZR) data during CAO conditions at the DOE Atmospheric Radiation Measurement (ARM) North Slope Alaska (NSA) site as input into the new retrieval, with the results compared to other available operational retrievals in Appendix A1.

2. Data and Methods

The two main retrieval methods are physical and statistical. One popular physical retrieval is an optimal estimation method, in which *a priori* data provide the first guess, and a forward model is used to perform gradient descent until converging on a complete atmospheric state (Maahn et al. 2020). The approach provides a quantified error characterization based on Bayes theorem (Maahn et al. 2020). Optimal estimation approaches are computationally expensive, prohibiting calculation of near-real-time LWP and water vapor path (WVP) estimates.

An optimal estimation approach depends on a significant *a priori* dataset of representative soundings, potentially drawn from model data. ERA5 reanalysis data have been used to develop WVP and LWP retrievals for other Arctic campaigns (e.g., Walbröl et al. 2022), but ERA5's dx = ∼31 km is not fully adequate for resolving CAO convective cells. Radiosondes are routinely launched from Jan Mayen and Bjornoya islands in the Norwegian Sea, but their data sampling of CAO conditions remains limited. Statistical retrievals, which can also be developed from radiosonde databases, rely on a previously-developed empirical relationship between the measurement and desired atmospheric variable. Statistical retrievals can use both linear and nonlinear regressions, or empirical orthogonal

functions. While computationally efficient, most statistical retrievals struggle to accurately represent complex relationships between variables (Maahn et al. 2020), and are strongly influenced by the initial developmental dataset. In addition, most statistical retrievals do not rigorously account for error propagation.

A statistical retrieval method that solves most of those shortcomings is machine learning. Machine learning has the advantage that complex nonlinear relationships between variables can be understood. In one example, Cadeddu et al. (2009) trained a neural network using GVR measurements and radiosonde data at the DOE ARM NSA site. This algorithm worked comparably well (or better) than other retrieval techniques in use at the same site. A drawback preventing its application to the CAESAR dataset is that none of the retrievals account for scattering by snow, and can only be applied to the same conditions the surface-based retrievals were developed for.

In this study, we build upon Cadeddu et al. (2009) by adding vertically-integrated 95 GHz radar reflectivities provided by the Wyoming Cloud Radar (WCR; version 4) as an additional input to articulate the influence of large particle scattering upon the LWP retrieval. The scattering is primarily due to snow for Arctic CAOs. The radar reflectivity is extremely sensitive to snowfall through its dependence on the sixth power of the particle size, and this can inform on the snow's contribution to the GVR brightness temperatures (T_b), as opposed to cloud liquid and water vapor alone. In addition, we provide robust error estimation for each individual retrieval value, by assessing the propagation of different error sources into the retrieval. While this retrieval is developed for pragmatic near-real-time application during the CAESAR campaign, the methods can be adapted for other applications as long as a representative model training data is available.

a. Instruments

The GVR measures sky radiances in four sidebands surrounding the 183.33 GHz water vapor absorption band: ±1 GHz, ±3 GHz, ±7 GHz, and ±14 GHz. The instrument is calibrated using a warm target whose temperature fluctuates around 15°C and a hot load kept near 60°C. The measurement error will increase with distance from the calibration temperatures and their difference, impacting the cold ±14 GHz T_b measurement the most. The ±1 GHz sideband is 30 times more sensitive to WVP than the T_b measured at 23.8 GHz by the more commonly used two-channel microwave radiometer (MWR) at WVP < 2.5 kg m^{-2} (Cadeddu et al. 2009). The ±7 GHz and ±14 GHz wing channels are 2-3.5 times more sensitive to LWP than the 31.4 GHz channel of a conventional MWR (Cadeddu et al. 2009; Zuidema et al. 2012). In more moist conditions, the channels nearest to the absorption band begin to saturate; however, the furthest wing channels retain sensitivity to moisture and cloud water for WVPs below 20 kg m^{-2}. We expect the thermodynamic conditions characterizing the wintertime CAOs over the Norwegian Sea to support useful LWP retrievals. The high T_b sensitivities to small amounts of integrated liquid and vapor make the GVR an ideal instrument for observing LWP and WVP in a cold, relatively dry environment supporting super-cooled liquid.

The airborne GVR, documented in Pazmany (2007), was first developed for use on the University of Wyoming King Air research aircraft (Wang et al. 2012), modified from a surface-based design built for northern Alaska (Cadeddu et al. 2009). The airborne GVR was subsequently leased from the manufacturer ProSensing for fieldwork in the southeast Pacific held in 2008 (Zuidema et al. 2012). The next deployment of the GVR was for the CAESAR campaign. The GVR was examined and calibrated prior to the deployment at the manufacturer, and outfitted with a new data computer. The GVR was also brought to the ARM SGP site in October-November 2023, where its measured T_b could be compared with that calculated from nearby radiosondes. This is discussed in Section 3. During the CAESAR deployment, oscillations occurred in the GVR T_b with a period of ~30-60 seconds and amplitudes that occasionally exceeded 10 K. These were associated with the internal warm load heater turning on. For most below-cloud legs during CAESAR, the heater was turned off to eliminate the oscillations. However, many of the above cloud WVP retrievals have oscillations of ~250-500 g m^{-2} because of the heater-induced T_b oscillations.

The WCR-4 (University of Wyoming - Flight Center 1995) has three directional antennas, of which we use only the upward-pointing single-polarization beam. The uncertainty in the absolute calibration of reflectivity is approximately 2.5 dB. The aircraft motion contribution into the beam is removed from the Doppler velocities to produce hydrometeor radial velocity. When flying straight and level, this is primarily the vertical velocity of hydrometeors, which consists of particle terminal velocity and vertical air motion.

The cloud temperature is also used in the retrieval, as the liquid water absorption coefficients vary with temperature. The cloud base temperature is estimated from the lifting condensation level calculated from the *in situ* ambient pressure, temperature, and dew point at flight level, serving as a proxy for the cloud temperature.

The LWP retrieval was compared to vertically-integrated *in-situ* liquid water contents (LWCs) derived from a King probe and *in-situ* cloud droplet size distributions spanning 3 to 50 μm in diameter from the inboard Cloud Droplet Probe (CDP) (Lance 2012). These were gathered during spiral profiles. The WVP retrieval was validated using the Buck hygrometer. These comparisons are explained further in Section 6.

b. LES and LAM Simulations of CAOs

The retrieval is trained on numerical simulations using the Weather Research and Forecasting (WRF) model (Skamarock and Klemp 2008; Skamarock et al. 2019). We use LAM simulations of three different CAOs sampled during the COMBLE campaign: 28 March 2020, 10 April 2020, and 26 April 2020. The LAM is configured using a nested, two domain setup (one-way feedback), with the outer and inner domains resolved with dx = 3 km and dx = 1 km, respectively. For this study, we use outputs from only the 1-km domain (light blue box in Fig. 1). The Mellor-Yamada-Nakanishi-Niino eddy-diffusivity/mass-flux planetary boundary layer (PBL) parameterization (Olson et al. 2019) is activated for the 28 March case, while the Yonsei University (YSU) PBL parameterization (Hong et al. 2006) is activated for the other two cases. The use of different PBL schemes yields a broader training dataset. In addition, the LAM simulation uses the Thompson-Eidhammer aerosol-aware microphysics parameterization (Thompson and Eidhammer 2014). This scheme can represent cloud condensation nuclei and ice nucleating particles prognostically (including precipitation scavenging). Recent advancements to the WRF model, as detailed by Juliano et al. (2022), enable the incorporation of time-varying aerosol fields from the GEOS-5 model. Additional details about the LAM configuration, including the physics parameterizations, may be found in Juliano et al. (2024).

To test the retrieval, we use model outputs from a separate WRF simulation of a 13 March 2020 CAO. This simulation consisted of a mesoscale domain (dx = 1050 m) coupled online (one-way feedback) to a very large LES domain, which resolved the Fram Strait at dx = 150 m (dark blue box in Fig. 1). The LES domain contained (3780,8400) grid cells in the (x,y) direction, thus spanning (567,1260) km in the (x,y) direction. First, the mesoscale domain was integrated from 12 to 22 UTC on 12 March, at which point the LES domain was activated, and the two domains integrated simultaneously while coupled online until 00 UTC on 14 March. The mesoscale domain uses the YSU PBL scheme and the LES domain uses the three-dimensional, turbulence kinetic energy-based subgrid-scale scheme of Deardorff (1980). For both domains, the vertical grid structure and other physics options, including the microphysics scheme, are identical to those settings for the LAM simulations.

Our four selected cases span a range of CAO conditions during COMBLE. For example, 26 April (closed cellular convection at the main COMBLE site) was one of the weaker cases observed during COMBLE and 10 April was a moderately strong CAO case (open cellular convection) (Lackner et al. 2024). Meanwhile, the 13 March (Fig. 1) and 28 March events were the two strongest observed during the COMBLE campaign, with large open cells (Lackner et al. 2024) and cloud top heights on 13 March reaching 3-5 km (not shown). These events were realistically depicted by the LAM simulations (Juliano et al. 2024). Underscoring the need to account for the snow's impact on the T_b, the snow water path (SWP) within a region of open celled convection (small red box in Fig. 1, spanning 15 km by 15 km) dominates the total water path (Fig. A2b).

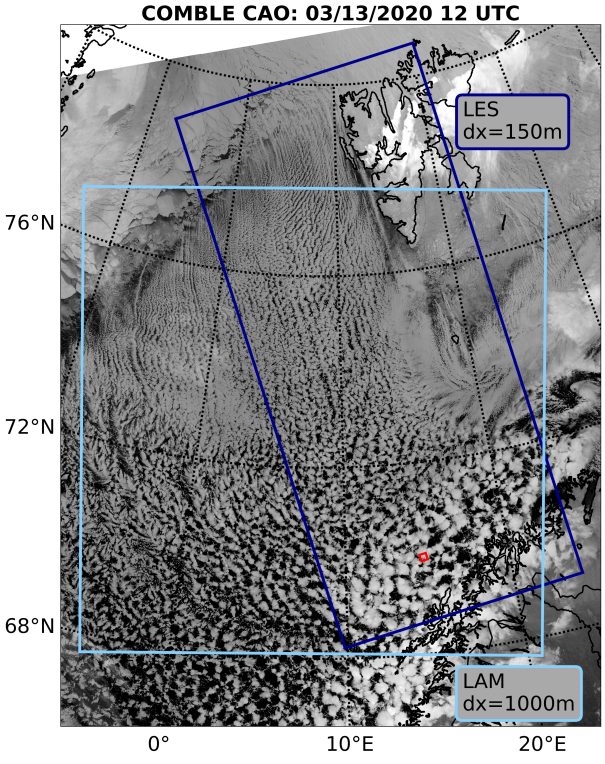

FIG. 1. NOAA-20 VIIRS infrared satellite image of a representative CAO cloud field at ~12 UTC during the 13 March 2020 case. The LES and LAM domains used in this analysis are shown in the light blue and dark blue boxes, respectively. The red box at 70°N, 15°E is detailed further in Fig. 2 and in Appendix A2.

c. PAMTRA

We use PAMTRA to calculate T_b and vertically-integrated radar reflectivities from the LES and LAM simulation outputs. PAMTRA is a forward radiative transfer model capable of simulating both active and passive microwave measurements (Mech et al. 2020) that has also been applied to data from other Arctic campaigns (e.g., Walbröl et al. 2024).

Figure 2 shows the output T_b at 183.3 ± 14 GHz and vertically-integrated 95 GHz reflectivities calculated by PAMTRA for the open-celled convection test section in Figure 1 after including all hydrometeors and water vapor, while Figure A2 indicates the contributions to T_b and reflectivity from the individual hydrometeors. Figures 2 and A2 are from only one snapshot of the LES simulation, but

represent the full simulation based on inspection of many such snapshots. Of the six hydrometeors considered (LWP, SWP, ice (IWP), graupel (GWP) and WVP), the LWP has the strongest influence on T_b (Fig. A2ai). Nevertheless, the T_b contribution from snow is also substantial (Fig. A2bi) and that from graupel (Fig. A2di) cannot be neglected. The contributions to radar reflectivity are dominated by snow (Fig. A2bii) and graupel (Fig. A2dii). Rain is infrequently present in CAOs over the Norwegian Sea during the late winter/early spring, and ice crystals contribute negligibly to both the T_b and radar reflectivities (Figs. A2ci,cii).

From Figure A2, we can infer that the microphysical representation of the snow is important to both the T_b and radar reflectivity. The user interface of PAMTRA allows for a variety of microphysical schemes, and supports a fine-tuning towards the anticipated microphysics. Adjustable parameters include the axial ratio (AR; the ratio of the major and minor axes of a hydrometeor), the area-size and mass-size relationships for frozen, non-spherical hydrometeors, and gamma distribution descriptions of all the particle size distributions, using a shape parameter μ to establish the distribution widths. The relationship between a hydrometeor's diameter, D, and mass, M, is defined through a power law with a prefactor, a, and power, b, as $M = aD^b$. The value of b will vary between 2 (for a thin circular plate) to 3 (for a perfectly spherical hydrometeor). Similarly, the projected surface area, A, relates to D as $A = \alpha D^\beta$. The microphysical parameters chosen for the hydrometeor species most impactful for the LWP retrieval are summarized in Table 1. The T_b from the liquid water is not impacted by the size distribution of cloud droplets as long as the radiative transfer falls within the Rayleigh regime. This is satisfied as long as the drop sizes remain smaller than 1.5 mm, given that the GVR wavelength is at 183.3 GHz. The radar reflectivity is nevertheless affected weakly by the shape parameter, μ. We use a μ = 9.6 for cloud droplets based on Miles et al. (2000).

PAMTRA uses the self-similar Rayleigh-Gans approximation for simulating frozen hydrometeors. For snow and graupel, the largest uncertainty in simulated T_b and reflectivity is from the choice of the mass-size parameters, a and b. The mass-size and area-size relationships are both highly dependent on the amount of riming, which varies significantly spatially and temporally. As a particle's rime fraction increases, it becomes more spherical and more dense. Using this knowledge, Mason et al. (2018) developed a line of best fit from past research campaigns of a versus b and α versus β along a continuum of density factors (ρ) stretching from ρ = 0 for unrimed aggregates measured in cirrus clouds (Brown and Francis 1995), to ρ = 1 for spheres of solid ice. A snow density factor of ρ = 0.2 and a graupel density factor of ρ = 0.7 are used to calculate a, b, α, and β using Mason et al. (2018). In addition, the AR value depends on the specific dominant

	AR	a	b	α	β	μ
Cloud Droplet	1	n/a	n/a	n/a	n/a	9.6
Snow	0.6	0.0908	2.12	0.0878	1.774	-1
Graupel	1	14.01	2.67	n/a	n/a	5

TABLE 1. Microphysical parameters used for the different hydrometeors simulated in PAMTRA: The axial ratio (AR), mass-size relation variables (a and b), area-size relation variables (α and β), and the shape parameter (μ).

snow morphology. We specify an AR = 0.6 for snow following Mason et al. (2019) and note that the reflectivity is not sensitive to AR variations near that value (Mason et al. 2019).

The final important microphysical choice is the shape parameter, μ, for snow and graupel. Mason et al. (2018), using a triple radar retrieval of snow-containing clouds in Finland, document μ = -1 for snow (in agreement with Brandes et al. 2007), and μ = 5 for graupel. Values of $\mu > 0$ generate a distribution that is broader than an exponential distribution, while a distribution with $\mu < 0$ is narrower than an exponential distribution. Higher μ values increase the number concentration of large hydrometeors relative to small ones, which especially affects radar reflectivity.

Graupel is represented using a single moment in the LES/LAM simulations. We set the effective radius to 0.7 mm. This value falls on a plateau region in the dBZ versus effective radius relation (Sieron et al. 2017), and a small change in the effective radius choice doesn't noticeably impact the calculated reflectivity.

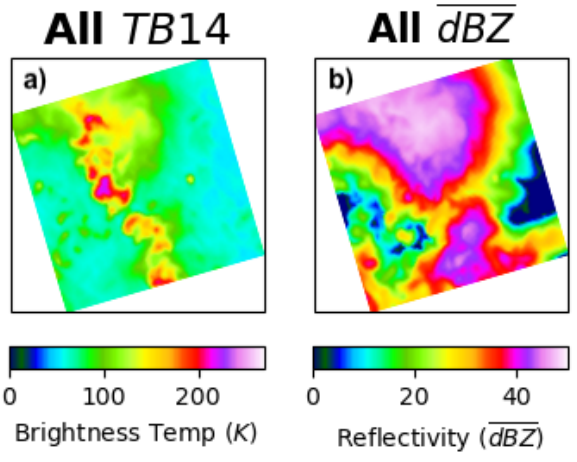

FIG. 2. PAMTRA-simulated (a) 183.3 ±14 GHz T_b and (b) vertically-integrated 95 GHz reflectivities ($\overline{dBZ}$) from all hydrometeors within the open-celled test section (red box in Fig. 1).

d. Data Preprocessing

The sampling of every gridpoint from the LES and/or LAM models is not practical due to the runtime constraint

on PAMTRA. Cloud liquid and snow are the primary heterogeneously-distributed variables influencing T_b and reflectivity. Therefore, we apply a weighted random selection method to the training/test points over the ocean, such that their two-dimensional histogram (LWP x SWP) span the full range of anticipated conditions. This also increases the range of WVPs sampled while reducing the sampling of clear-sky points, and optimizes sampling of a variety of conditions. Testing/training points vary both horizontally across the model domain and vertically from 0 to 5000 m. This sampling method is applied to both the LAM and LES model output. There are approximately 600,000 training points and 100,000 testing points.

1) Radar Integration

The four radiometer measurements are sensitive to the full atmospheric column with the presence of snow introducing uncertainty within the LWP and WVP retrievals. In keeping with this low-dimensionality, the radar reflectivities are vertically-integrated, producing a single value at each spatial gridpoint, using $\overline{dBZ} = 10 * log_{10} \int_{z_i=FL}^{z_i=TOA} Z_{e,i}\, dz$, where $Z_{e,i} = 10^{\frac{1}{10} dBZ_i}$. Any final integrated reflectivity less than -20 dBZ was set to -20 dBZ.

2) Cloud Temperature Weighting

Cloud temperature impacts the retrieved T_b through the strong temperature dependence of the liquid dielectric constant: colder clouds emit more at microwave frequencies than do warmer clouds (Westwater et al. 2001; Zuidema et al. 2005a). We follow Turner et al. (2007) and normalize the simulated T_b using the lifting condensation level (LCL) temperature as a proxy for the cloud temperature, through $T_{b,normalized} = \frac{273}{LCL_{temp}} T_b$ with the LCL temperature (LCL_{temp}) in Kelvin. In both the model and flight data, the LCL is calculated from the thermodynamic values at the flight altitude, simulated or real-time. Any LCL temperature below 243 K is set to 243 K (because little liquid is expected at cloud temperatures colder than 243 K).

Without this correction, the retrieved LWPs do not compare as well to either the model values or *in-situ* measurements made during CAESAR (not shown). The normalized T_b is only applied to the LWP retrieval as the water vapor gaseous absorption constants are not highly temperature-dependent.

e. Machine Learning Approaches

Two machine learning approaches, with different sensitivities to input errors, are applied in tandem and subsequently averaged to produce the retrieved LWPs and WVPs. One is a neural network regression and the other is a random forest regression. For both methods, the input is a vector of length 5 containing the 183.3 GHz ±14, ±7, ±3, and ±1 GHz T_b and the vertically-integrated 95 GHz radar reflectivity. Noise is not added to training data. The output is LWP or WVP. While this may suggest an overconstrained solution, we cannot control well for other influencing variables, such as the vertical structure of temperature and humidity. This is the reason for selecting model simulations of the same cloud regime for the training and validation datasets.

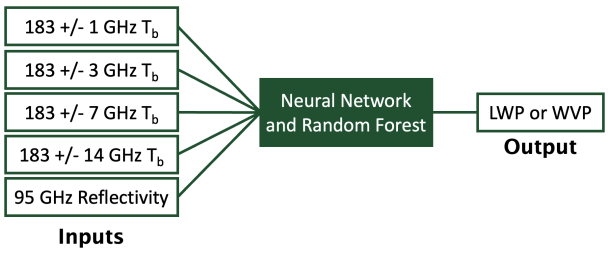

Fig. 3. Inputs and outputs of the machine learning retrieval. Neural network and random forest models are run separately and then averaged together. Note the reflectivity is a vertically-averaged quantity.

The neural network approach uses a Multilayer Perceptron Neural Network (MPLNN) based on the MPLRegressor model within the sklearn Python package. MPLNNs are used for complex regression tasks across many disciplines and can identify complex non-linear relationships between variables. We use a MPLNN with a Rectified Linear Unit (ReLU) activation function using 20 layers of 200 neurons. The MPLNN regression can extrapolate beyond the output phase space that it is trained on, supporting predictions with decent accuracy beyond the original phase space. The weakness of MPLNN is that extreme outlier predictions lying well outside the realm of reality can also result, if an instrument is poorly calibrated and/or produces measurements well outside the input training phase space.

The other machine learning approach is a Random Forest (RF) Regressor, also from the sklearn Python package. The RF Regressor uses an ensemble of decision trees generated through bootstrapping the training dataset. The output of each of the decision trees is then averaged to generate a prediction. We use ten decision trees. One disadvantage is that the RF Regressor can only predict within the range of output values it is trained on. However, this is also an advantage in that the approach can handle instrument error better than the MPLNN and will not predict LWPs or WVPs outside of a physically realistic range. This rationalizes the decision to construct the average of the two retrievals into the final estimate of LWP and WVP.

3. ARM Southern Great Plains GVR Calibration Testing

From October 30th to November 10th 2023, the GVR was deployed to the DOE ARM Southern Great Plains

(SGP) site to take advantage of their regular, near-by radiosonde launches and other ancillary measurements. The T_b measured by the GVR during clear-sky conditions, determined using the Total Sky Imager (Flynn and Morris 2023), are compared to those simulated by PAMTRA based on the SGP radiosondes (Keeler et al. 2023) in Figure 4. Overall, the clear-sky GVR T_bs are warmer than those simulated by PAMTRA, especially under drier conditions and by the far wing channels, by up to 15 K (Fig. 4a).

The PAMTRA simulations rely on the Rosenkranz (1998) water vapor emission model. A sensitivity test relying on the MonoRTM (Clough et al. 2005) emission model slightly decreases the simulated T_b (increasing the bias relative to the GVR), by approximately 1-2 K. This small difference between radiative transfer models indicates most of the discrepancy is from a miscalibration of the GVR.

The best-estimate of the bias as a function of the measured T_b (black solid line in Fig. 4b) is used to post-process the GVR T_bs during CAESAR. The bias correction also improved a high bias noted in the real-time retrieved LWP and WVP estimates during the campaign.

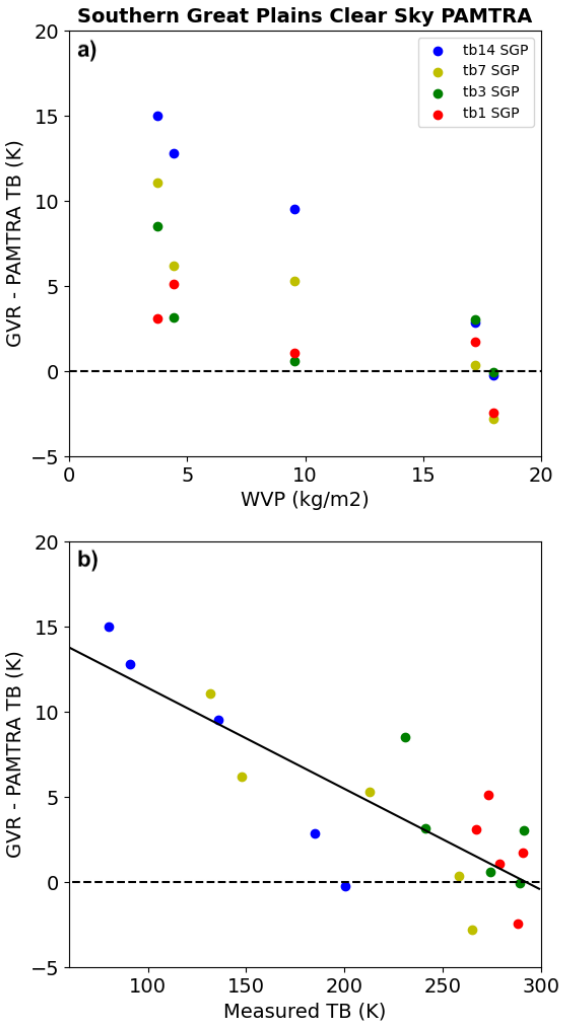

FIG. 4. Bias of GVR T_bs in clear sky conditions using radiosonde data with respect to PAMTRA simulated T_bs at the ARM SGP field site plotted with a) radiosonde observed WVP as the dependent variable, and b)measured T_b as the dependent variable.

4. Machine Learning Model Testing

Training is conducted on selected points from LAM simulations of three independent CAOs emcompassing the full range of possible conditions over the Norwegian Sea, referred to as PAMTRA-train. The test dataset, a PAMTRA simulation of an LES run of a CAO from 13 March 2020, is referred to as PAMTRA-test.

a. Control

The control test determines the LWP and WVP for the PAMTRA-test cases based only on the simulated GVR T_bs and radar reflectivities. These values are then directly compared to model diagnostics (Fig. 5a-b). The model performed well, with explained variances of 99% and 100% for the LWP and WVP retrievals, respectively. However, this assumes perfect information, and doesn't account for any sources of error. When the reflectivity is neglected within retrieval, the retrieved LWPs are clearly biased low, while the retrieved WVPs are only slightly worse (Fig. 5c-d).

b. Error Estimations

Several sources of error are not accounted for in the control test. These include the GVR instrument error, and error in the representation of the microphysical size distributions. Other errors are not considered.

Random instrument error is simulated by perturbing each PAMTRA-test T_b randomly using a normal distribution with a standard deviation of 2 K, the stated uncertainty of the GVR measurements (Cadeddu 2011). The random instrument error in WCR reflectivity is ignored because its impact is an order of magnitude smaller than changes to the reflectivities caused by altering the snow/graupel characteristics. Errors within the mass-size and area-size relationships of snow and graupel are evaluated by perturbing the snow/graupel density factors within separate PAMTRA simulations of the 13 March 2020 LES case, leading to different mass-size and area-size relationships. The density factor ρ is perturbed by $\pm$ 0.1 from the settings within PAMTRA-test, corresponding to less riming (ρ_{snow} = 0.1 and $\rho_{graupel}$ = 0.6) and more riming (ρ_{snow} = 0.3 and $\rho_{graupel}$ = 0.8) than in the control run.

Performance metrics of WVP and LWP, shown in Tables 2-3 and Figures 5e-f, indicate the performance degrades as expected when errors are propagated into the retrieval, but

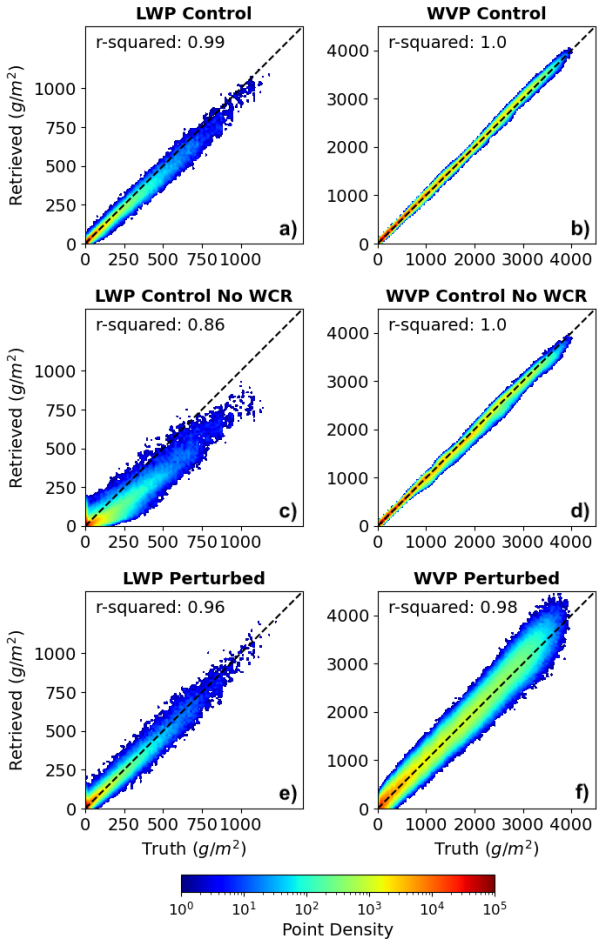

FIG. 5. Performance of both the LWP and WVP retrievals in a) and b): the control test; c) and d): the control test with reflectivity excluded from both the training or testing; e) and f): with perturbed instrument simulations and microphysics.

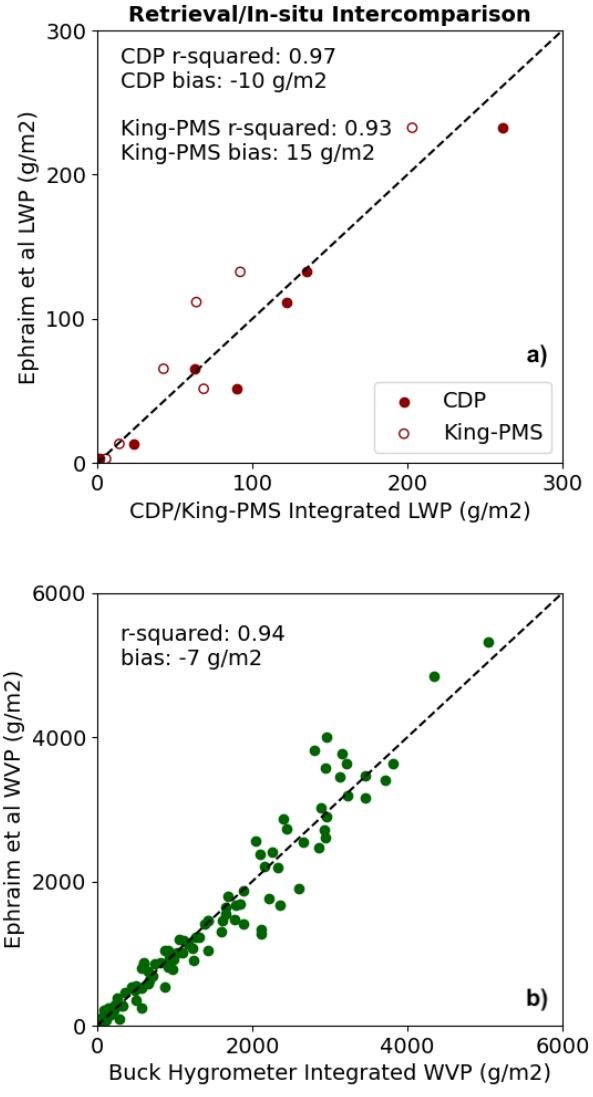

FIG. 6. a) Comparison of integrated *in-situ* LWC (using the CDP and King-PMS probes) compared to the retrieved LWP below the cloud base. Comparison is done after constant LWP bias correction is applied. b) Comparison of integrated *in-situ* specific humidity (using both Buck Model 1011C dew-point hygrometers) over a layer compared to the difference in retrieved WVP from the top to bottom of that layer.

much of the skill is still retained. In the LWP retrieval perturbed test, absolute errors increase as the LWP grows; however, the percent error decreases. Retrievals for LWPs greater than 100 g m^{-2} have a ~10% error. For WVPs, the perturbations produce < 10% error except in the driest conditions.

5. Implementation During CAESAR

The new retrieval supported real-time LWP and WVP estimates during CAESAR, with a time latency of less than 10 seconds on-board the plane. An on-board dashboard developed by the first author showed GVR T_b, WCR integrated reflectivity, LWP and WVP retrievals, plane altitude and air temperature on a display updating to the most recent 30 minutes of data. This included a real-time retrieval uncertainty from instrument uncertainties and a riming uncertainty, similar to the initial retrieval tests.

The near-real-time LWP estimates available during the below cloud legs helped inform how much icing might be experienced on the subsequent ascent. The estimates also aided a robust understanding of environmental and cloud conditions helpful for the other instrument teams. The real-time WVP was often useful for determining boundary layer growth, and for identifying sharp moisture boundaries designating different air masses, enabling decisions to resample a given area.

CAESAR also provided an excellent, independent opportunity to validate the GVR-based retrieval. LWCs from

LWP Performance (gm^{-2})

	25-50	50-100	100-250	250-500	500-1000	> 1000
Control RSME	8.2	11.0	20.1	47.1	79.8	97.0
Control % Error	17.9%	11.5%	9.8%	11.3%	10.6%	7.4%
Perturbed RMSE	18.0	19.4	26.6	47.1	73.8	104.9
Perturbed % Error	39.4%	21.2%	13.3%	10.9%	9.3%	7.5%

TABLE 2. Performance metrics (root-mean-square error as absolute and a percentage) for both control and perturbed LWP datasets binned by the truth LWP.

WVP Performance (g m^{-2})

	250-500	500-1000	1000-2000	2000-3000	3000-4000	>4000
Control RMSE	21.3	28.2	31.2	48.6	60.8	21.9
Control % Error	5.1%	3.3%	1.8%	1.6%	1.6%	0.5%
Perturbed RMSE	110.9	128.1	154.9	198.6	256.8	396.3
Perturbed % Error	24.8%	14.5%	8.6%	6.5%	6.3%	7.4%

TABLE 3. Performance metrics (root-mean-square error as absolute and a percentage) for both control and perturbed WVP datasets binned by the truth WVP.

the CDP and the King probe were integrated from ascents and descents through clouds, and compared to the three-minute averages of retrieved LWP during the adjacent below-cloud leg. Due to the heterogeneous distribution of cloud water, the comparison relies only on spiral ascents and descents through homogeneous cloud (or clear-sky) layers. Eight spiral ascents/descents (two clear sky and six through cloud) met this criteria across four research flights (RF02, RF04, RF06, and RF07, occurring on 29 February 2024, 3 March 2024, 12 March 2024, and 16 March 2024 respectively).

In contrast, water vapor is more horizontally homogeneous than cloud LWC, and almost all aircraft profiles contributed to the comparison. Clear and cloudy sky profiles totaled 97 ascents/descents across all research flights. The WVP constructed from best-estimate specific humidities as measured by a Buck hygrometer during ascents/descents is compared to the retrieved WVP difference between the bottom and top of the ascent/descent.

Initially, a large high bias in LWP (~75 g m^{-2}) and WVP (~200 g m^{-2}) was observed when comparing to the *in-situ* probe data. This is consistent with a sensitivity of ±14 GHz T_b to LWP of ~0.206 K/g m^{-2} (Ulaby et al. 1986), suggesting a bias in the ±14 GHz T_b of around 15 K - of a similar magnitude observed at ARM SGP. After adjusting the T_bs using data presented in Figure 4 from the ARM SGP site, the bias in the LWP retrieval reduced to ~25 g m^{-2} and the WVP bias disappeared. Based on this assessment and sanity checks in the clear-sky situations, a constant offset of 25 g m^{-2} was further removed from each retrieved LWP.

Figure 6 shows the comparison to the *in-situ* measurements after these bias corrections were incorporated. The correlations of the LWP retrieval to integrated *in-situ* LWPs is high, with an explained variance of 93-97% (Fig. 6a). The final bias becomes -10 and +15 g m^{-2}, relative to the CDP and King probes, respectively. The King probe is known to underestimate the contribution of the larger drop sizes (Lance 2012), while the CDP probe is calibrated with glass beads and has a sizing uncertainty of 10-20% (Lance et al. 2010). As such the GVR LWP estimates can be considered to be within the bounds of the uncertainties of the two cloud probes.

6. Selected Results

A variety of conditions were experienced during the near-surface legs during CAESAR (Fig. 7). Most CAO clouds possess LWPs below 200 g m^{-2}, but the strongest convective updrafts in open celled convection may contain LWPs approaching or exceeding 1000 g m^{-2}. Such updrafts may contain drops of sufficient size that Mie scattering increases the T_b, unphysically increasing the retrieved LWPs (Cadeddu et al. 2017). Such high retrieved LWPs will receive further scrutiny. WVPs vary from flight to flight based on the background synoptic conditions, ranging from 1000 g m^{-2} to 7000 g m^{-2}.

An example from 29 February (RF02) is shown in Figure 8, during which a closed to open celled transition is sampled. Pitch/roll angle is accounted for by correcting for the increased path length. During the closed cell regime, LWPs are relatively constant around 200-300 g m^{-2}. After the transition to open cells, LWPs are much more variable, with maximum LWPs exceeding 500 g m^{-2}, aligning with updrafts. In other areas, the cloud is mostly or completely glaciated. An in-depth analysis of this case will be saved for a future paper.

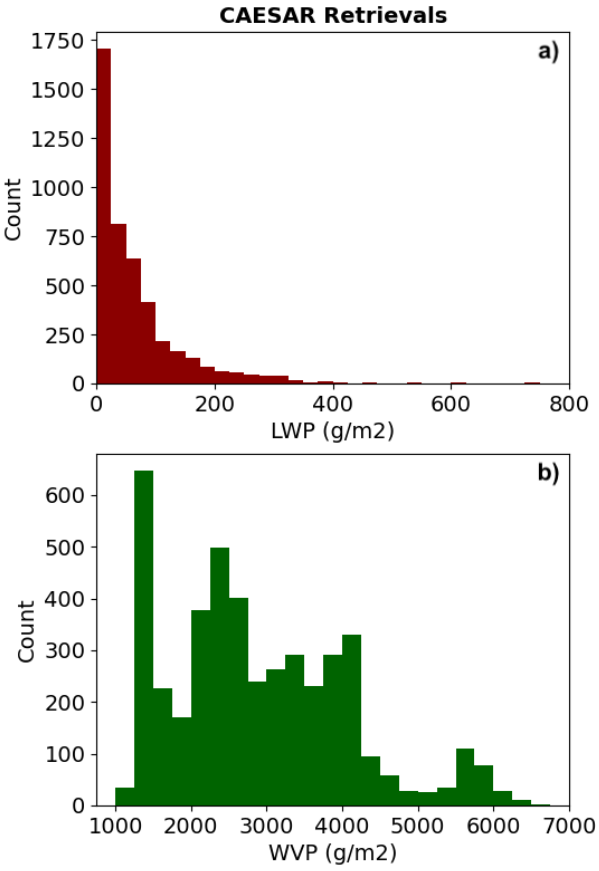

FIG. 7. Histogram of retrieved LWP and WVP during CAESAR when the C-130 was below 500m altitude and GVR oscillations were not present (including clear sky times). Polar low flight, RF09, is not included.

7. Conclusion

This retrieval method successfully diagnosed the LWP and WVP along the flight tracks during the CAESAR campaign. While this demonstration highlights the benefits of multi-instrument retrievals, there are still some areas for improvement. For example, in thin clouds, in some instances the retrieval is too sensitive to changes in WCR reflectivity, causing it to diagnose small amounts of LWP (though zero is still within the margin of error) in clouds that are likely all ice based on the Wyoming Cloud Lidar (WCL) data (University of Wyoming - Flight Center 2007), and the lack of spikes in the GVR T_b time series. One example of this phenomena occurred near the sea ice edge during RF07. One possible cause is that the riming factor in the operational retrieval does not match the observed microphysics. After an analysis of the microphysical probes and particle imagery from CAESAR, adjustments may be made to the riming factor used. In addition, further work may explore integrating other upward-looking instruments into the retrieval, such as the WCL to better constrain the retrieval.

Despite any shortcomings, this retrieval agrees well with the cloud probes across multiple research flights (Fig. 6), and diagnoses LWP maximum within updrafts similar to other research in this regime (Mages et al. 2023). The approach can be adapted to a wide variety of applications as long as the training data accurately represents the mesoscale conditions the retrieval is applied to, and ideally will serve to support further characterization work of mixed-phase convective clouds.

Acknowledgments. SE and PZ gratefully acknowledge financial support through NSF AGS award number 2150848. We thank NCAR RAF and NSF for their dedication and commitment to the CAESAR project. All PAMTRA simulations were run on NSF NCAR High-Performance Computers, named Derecho and Cheyenne (Computational and Information Systems Laboratory (2024) and Computational and Information Systems Laboratory (2023)). We thank Davide Ori, Jan Chylik, and Mario Mech for their advice on the PAMTRA code.

Data availability statement. Datasets for the NSF-supported CAESAR campaign are publicly available through the National Center of Atmospheric Research Earth Observing Laboratory after April 7, 2025, with the data used for this publication available prior from the authors. Data were obtained for the Southern Great Plains and North Slope of Alaska sites from the Atmospheric Radiation Measurement (ARM) user facility, managed by the U.S. Biological and Environmental Research Program for the Department of Energy Office of Science (`https://www.arm.gov/`). The PAMTRA code is publicly available through a GitHub repository distributed under a GPLv3.0 license at `https://github.com/igmk/pamtra`. Files related to the WRF model setup, raw and post- processed WRF outputs, satellite retrievals, and analysis scripts are available in a Harvard Dataverse re- pository (https://doi.org/10.7910/DVN/U3VI1X; Juliano I& Lackner, 2024).

APPENDIX

A1. ARM North Slope Alaska Site Testing

The retrieval was further tested on data from the ARM NSA site in Utquigvik, Alaska (formerly Barrow). CAO conditions are frequent in Utquigvik during October, when the Beaufort Sea is still ice-free (Wang et al. 2016). The presence of CAOs at the ARM NSA site is identified using the M index, defined as $M = \theta_{SST}$ - θ_{850hPa} where θ is potential temperature (Kolstad and Bracegirdle 2008), SST corresponds to the average SST over a 2° latitude by 4° longitude box due north of the NSA site using the

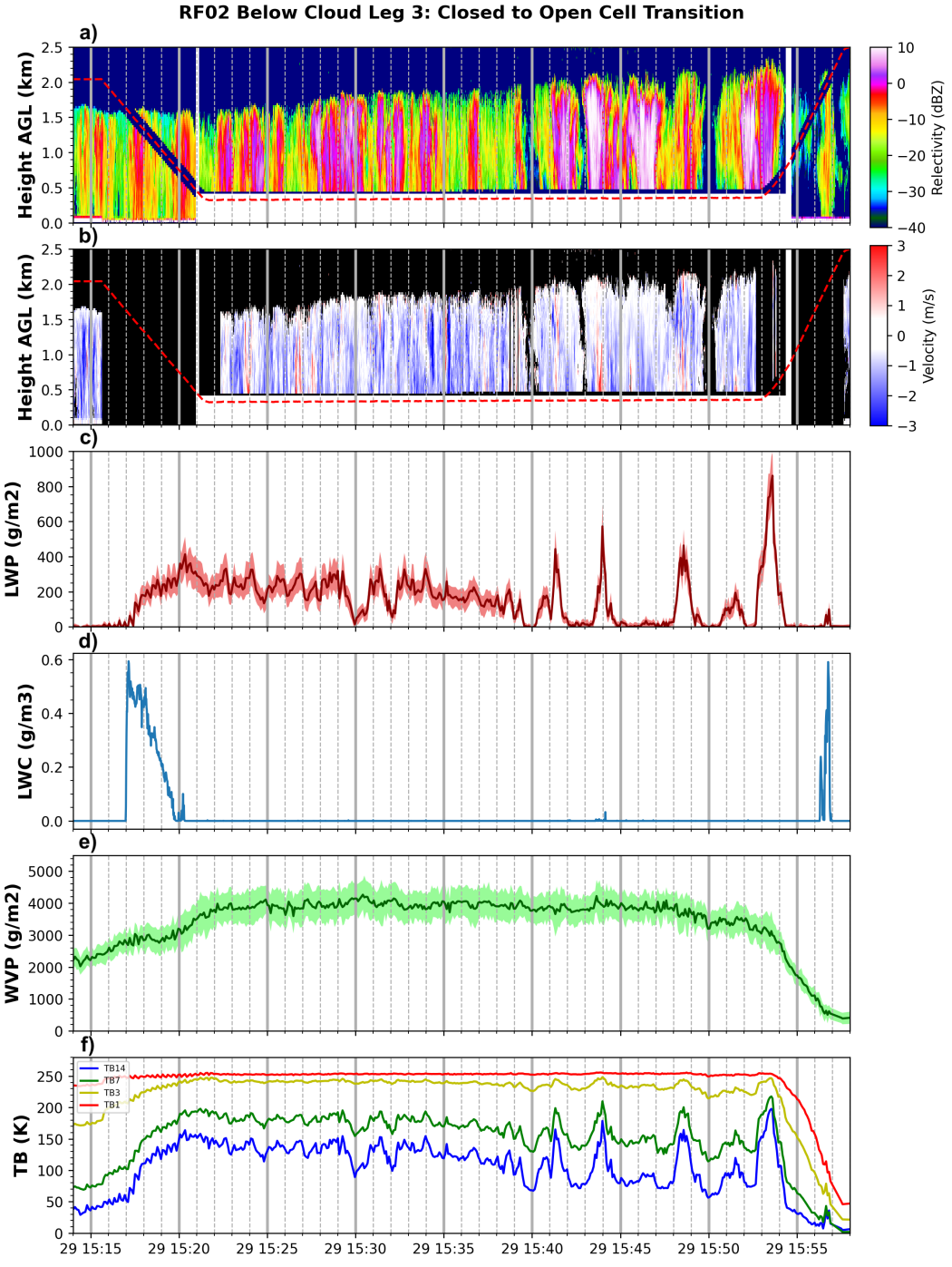

FIG. 8. Retrievals during a below cloud leg from RF02 on February 29th 2024. This leg samples across a closed to open celled transition. Dotted red line in the the WCR reflectivity (a) and Doppler velocity (b) plots shows the plane's altitude with time. Uncertainties in the retrievals are represented as the shaded area surrounding the dark lines for the LWP (c) and WVP (e) retrievals. Cloud droplet probe (CDP) *in-situ* measurements of LWC (d) are also shown. Non-normalized GVR T_bs are shown in (f).

NOAA/NCEI 1/4° Daily Optimum Interpolation Sea Surface Temperature (OISST; Reynolds et al. 2007). The 850 hPa temperature is identified from the NSA radiosondes (Keeler et al. 2023). When M is positive, the atmosphere

is thermally unstable. An additional criterion is that the sea ice concentration, based on the NCEP and GSFC sea ice product, is < 33% in the same box. These criteria identified six CAOs spanning a total of 104 hours from 2020 and 2021 that were used to test the retrieval.

The site includes a surface-based GVR radiometer (Cadeddu and Tuftedal 2021), a 35 GHz Ka-band ARM Zenith Radar (KAZR) (Feng et al. 2021), and independent LWP and WVP retrievals to compare against. Surface pressure, 2m temperature, and 2m dew point determine the temperature at the LCL, serving as a proxy for the cloud base temperature within the retrieval. For this test, PAMTRA is used to simulate the LAM training case reflectivities to match the 35 GHz KAZR. All other methods used are the same. The three independent retrieval methods include Turner et al. (2007) and two different retrievals from Liljegren (2004). Turner et al. (2007) is an optimal estimation retrieval utilizing both infrared and microwave (MWR) measurements, and relies on the MonoRTM code. Liljegren (2004) are statistical retrievals based on measurements from a a 12-channel profiler radiometer (MWRP), and on only two channels of the MWRP. Liljegren (2004) uses the Rosenkranz (1998) water vapor absorption model.

Comparisons to the three other retrievals indicate relatively good agreement (Fig. A1). We note that even though the Turner et al. (2007) and Liljegren (2004) retrievals are well established, this comparison is still different from comparing to truth. Inherent errors may be common to all the retrievals in addition to the instruments. Nonetheless, this comparison acts as a high quality sanity check.

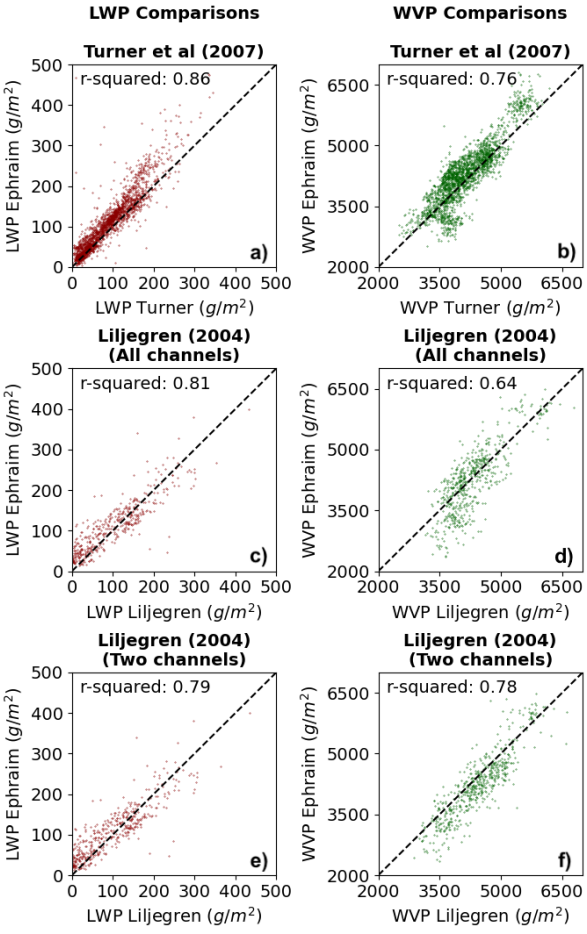

FIG. A1. Comparison of our LWP and WVP retrievals to other retrievals in use at the ARM NSA site.

A2. Qualitative Demonstration

The main premise of using radar reflectivities in our retrieval of LWP while previous retrieval methods typically only use radiometers is that liquid cloud droplets are not the only hydrometeor contributing to measured T_b. Cloud liquid contributes to brightness through primary emission, but snow also has a secondary contribution to brightness by scattering upward emissions from the ocean back downward to the radiometer. To demonstrate this relationship, we looked at PAMTRA simulated T_bs and reflectivities in a 15x15 km box of the LES model run in a region of open cell convection that contained the highest LWPs. This region is outlined in a small red box in Figure 1. The hydrometeor amounts of each species are shown in the first column in Figure A2. The hydrometeor species shown are LWP, SWP, ice water path (IWP), graupel water path (GWP). Water vapor path (WVP) is also evaluated. Rain water path is not included as rain is not often present in CAOs in the Norwegian Sea during the timeframe of CAESAR.

To simulate the GVR, we used PAMTRA to find T_b contributions from each individual hydrometeor species at (183.3 ± 14 GHz) from the same 15x15 km section of the LES model that is shown in the second column of Figure A2. The ±14 GHz channel was chosen since water vapor has the smallest impact on that channel, allowing for a more vivid comparison. The primary contribution to total T_b is cloud liquid, the secondary contribution is by snow. Other hydrometeor types have negligible effects.

To simulate the WCR, we used PAMTRA to find the vertically integrated 95 GHz reflectivities of each individual hydrometeor species in the 15x15 km box. The primary contribution to reflectivity is due to snow, with a secondary contribution from cloud liquid. The third column in Figure A2 shows integrated reflectivities.

Cloud ice is present in low quantities, and graupel is present in very scattered locations. Nonetheless, we attempted to estimate the total amount of frozen hydrometeors (frozen water path, FWP = snow + graupel + cloud ice) as that is a more useful quantity than snow alone. In addition, the threshold separating snow from cloud ice in the model output is an arbitrary size with little physical significance. Overall, this demonstrates that a retrieval of LWP and FWP should be achievable. This is because while con-

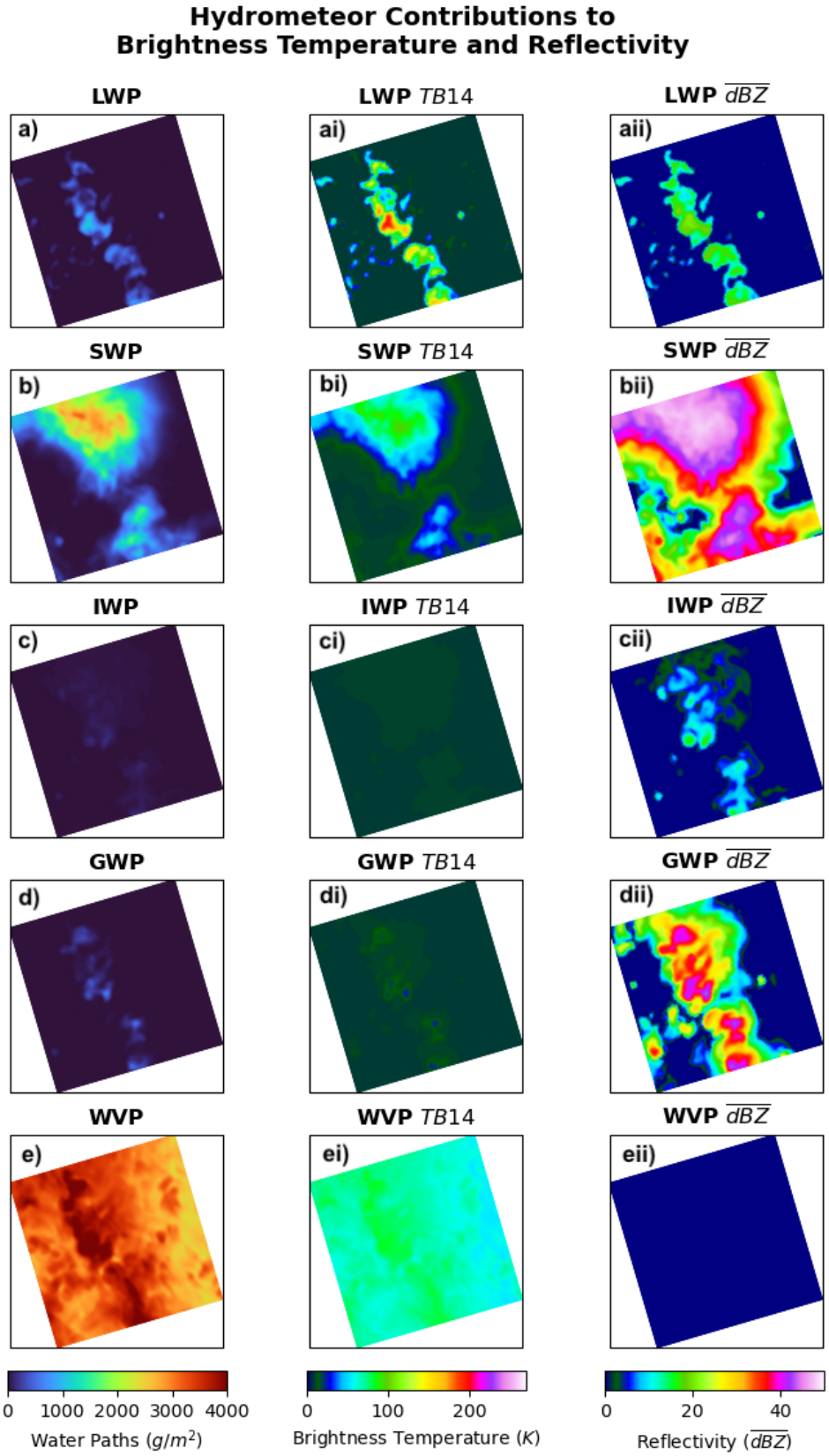

FIG. A2. The first column shows the spatial distribution of a) LWP, b) SWP, c) ice water path (IWP), d) graupel water path (GWP), and e) WVP within the red box in Fig. 1. This is a region of CAO open celled convection in an LES model simulation of 13 March 2020. The second column shows contribution of ai) LWP, bi) SWP, ci) IWP, di) GWP, and ei) WVP to the ±14 GHz T_b. The third column shows contribution of aii) LWP, bii) SWP, cii) IWP, dii) GWP, and eii) WVP to the integrated 95 GHz reflectivities ($\overline{dBZ}$).

ducting a retrieval, we will have two unknown variables (LWP and FWP) and two known independent variables coming from measurements of the GVR and WCR. Both LWP and FWP have distinct patterns in how they impact GVR and WCR measurements. Cloud liquid dominates the GVR T_b and has a secondary contribution to WCR reflectivity. Frozen hydrometeors dominate WCR reflectivity and have a secondary contribution to GVR T_b. Unfortunately, a retrieval of FWP only worked in model testing and was not reliable in the field. This is likely due to the high sensitivity of the FWP retrieval to PAMTRA modeled reflectivities. Even small differences between the training and observed reflectivities (caused by differences in the calibration of the WCR with respect to PAMTRA simulations and our representation of the frozen microphysics in PAMTRA) were too large for a viable FWP retrieval.

References

Abel, S. J., and Coauthors, 2017: The role of precipitation in controlling the transition from stratocumulus to cumulus clouds in a northern hemisphere cold-air outbreak. *J. Atmos. Sci.*, **74 (7)**, 2293 – 2314, doi:10.1175/JAS-D-16-0362.1.

Bodas-Salcedo, A., T. Andrews, A. V. Karmalkar, and M. A. Ringer, 2016a: Cloud liquid water path and radiative feedbacks over the southern ocean. *Geophys. Res. Lett.*, **43**, 10,938–10,946, doi:10.1002/2016GL070770.

Bodas-Salcedo, A., P. G. Hill, K. Furtado, K. D. Williams, P. R. Field, J. C. Manners, P. Hyder, and S. Kato, 2016b: Large contribution of supercooled liquid clouds to the solar radiation budget of the southern ocean. *J. Climate*, **29 (11)**, 4213 – 4228, doi:10.1175/JCLI-D-15-0564.1.

Brandes, E. A., K. Ikeda, G. Zhang, M. Schönhuber, and R. M. Rasmussen, 2007: A statistical and physical description of hydrometeor distributions in colorado snowstorms using a video disdrometer. *Journal of Applied Meteorology and Climatology*, **46 (5)**, 634 – 650, doi:10.1175/JAM2489.1, URL https://journals.ametsoc.org/view/journals/apme/46/5/jam2489.1.xml.

Bremen, L. V., E. Ruprecht, and A. Macke, 2002: Errors in liquid water path retrieval arising from cloud inhomogeneities: The beam-filling effect. *Meteor. Z.*, **11**, 13–19, doi:10.1127/0941-2948/2002/0011-0013.

Brown, P. R. A., and P. N. Francis, 1995: Improved measurements of the ice water content in cirrus using a total-water probe. *Journal of Atmospheric and Oceanic Technology*, **12 (2)**, 410 – 414, doi:10.1175/1520-0426(1995)012⟨0410:IMOTIW⟩2.0.CO;2, URL https://journals.ametsoc.org/view/journals/atot/12/2/1520-0426_1995_012_0410_imotiw_2_0_co_2.xml.

Cadeddu, M., and M. Tuftedal, 2021: G-band (183 ghz) vapor radiometer (gvr). Accessed 23 January 2024, doi:10.5439/1986620.

Cadeddu, M. P., 2011: Gvr radiometer handbook. Tech. rep., ARM.

Cadeddu, M. P., R. Marchand, E. Orlandi, D. D. Turner, and M. Mech, 2017: Microwave passive ground-based retrievals of cloud and rain liquid water path in drizzling clouds: Challenges and possibilities. *IEEE Trans. Geosci. Remote. Sens.*, **55**, 6468–6481.

Cadeddu, M. P., D. D. Turner, and J. C. Liljegren, 2009: A neural network for real-time retrievals of pwv and lwp from arctic millimeter-wave ground-based observations. *IEEE Transactiond on Geoscience and Remote Sensing*, **47**, 1887–1900, doi:10.1109/TGRS.2009.2013205, URL https://radiometrics.com/wp-content/uploads/2021/10/cadeddu_tgrs09.pdf.

Clough, S., M. Shephard, E. Mlawer, J. Delamere, M. Iacono, K. Cady-Pereira, S. Boukabara, and P. Brown, 2005: Atmospheric radiative transfer modeling: a summary of the aer codes. *Journal of Quantitative Spectroscopy and Radiative Transfer*, **91 (2)**, 233–244, doi:https://doi.org/10.1016/j.jqsrt.2004.05.058, URL https://www.sciencedirect.com/science/article/pii/S0022407304002158.

Computational and Information Systems Laboratory, 2023: Cheyenne: HPE/SGI ICE XA System (University Community Computing). Boulder, CO: NSF National Center for Atmospheric Research. doi:doi:10.5065/D6RX99HX.

Computational and Information Systems Laboratory, 2024: Derecho: HPE Cray EX System (University Community Computing). Boulder, CO: NSF National Center for Atmospheric Research. doi:10.5065/qx9a-pg09.

Deardorff, J. W., 1980: Stratocumulus-capped mixed layers derived from a three-dimensional model. *Bound.-Layer Meteor.*, **18**, 495–527.

Feng, Y.-C., and Coauthors, 2021: Ka arm zenith radar (kazrcfrge). Accessed August 30 2023, doi:10.5439/1498936.

Flynn, D., and V. Morris, 2023: Total sky imager (tsiskycover). Accessed 10 January 2024, doi:10.5439/1992207.

Geerts, B., and Coauthors, 2022: The COMBLE campaign: A study of marine boundary layer clouds in arctic cold-air outbreaks. *Bull. Am. Meteor. Soc.*, **103 (5)**, E1371 – E1389, doi:10.1175/BAMS-D-21-0044.1.

Hong, S.-Y., Y. Noh, and J. Dudhia, 2006: A new vertical diffusion package with an explicit treatment of entrainment processes. *Mon. Wea. Rev.*, **134**, 2318–2341.

Juliano, T. W., C. P. Lackner, B. Geerts, B. Kosovic, L. Xue, P. Wu, and J. Olson, 2024: Simulating mixed-phase open cellular clouds observed during comble: Evaluation of parameterized turbulence closure. *J. Geophys. Res.: Atmos.*, **129**, doi:10.1029/2024JD040889, e2024JD040889.

Juliano, T. W., and Coauthors, 2022: Smoke from 2020 United States wildfires responsible for substantial solar energy forecast errors. *Environ. Res. Lett.*, **17**, 034010.

Keeler, E., K. Burk, and J. Kyrouac, 2023: Balloon-borne sounding system (sondewnpn). Accessed 23 January 2024, doi:10.5439/1595321.

Khanal, S., Z. Wang, and J. R. French, 2020: Improving middle and high latitude cloud liquid water path measurements from modis. *Atmos. Res.*, **243**, 105 033, doi:https://doi.org/10.1016/j.atmosres.2020.105033.

Kolstad, E. W., and T. J. Bracegirdle, 2008: Marine cold-air outbreaks in the future: an assessment of ipcc ar4 model results for the northern hemisphere. *Climate Dynamics*, **30**, 871–885, doi:10.1007/s00382-007-0331-0, URL https://doi.org/10.1007/s00382-007-0331-0.

Korolev, A., and Coauthors, 2017: Mixed-phase clouds: Progress and challenges. *Meteorological Monographs*, **58**, 5.1 – 5.50, doi:10.1175/AMSMONOGRAPHS-D-17-0001.1.

Korolev, A. V., J. W. Strapp, G. A. Isaac, and A. N. Nevzorov, 1998: The nevzorov airborne hot-wire lwc–twc probe: Principle of operation and performance characteristics. *J. Atmos. Oceanic Technol.*, **15**, 1495–1510, doi:10.1175/1520-0426(1998)015⟨1495:TNAHWL⟩2.0.CO;2.

Lackner, C. P., B. Geerts, T. W. Juliano, B. Kosovic, and L. Xue, 2024: Characterizing mesoscale cellular convection in marine cold air outbreaks with a machine learning approach. *J. Geophys. Res.*, **129**, doi:10.1029/2024JD041651, e2024JD041651.

Lance, S., 2012: Coincidence errors in a cloud droplet probe (cdp) and a cloud and aerosol spectrometer (cas), and the improved performance of a modified cdp. *Journal of Atmospheric and Oceanic Technology*, **29 (10)**, 1532 – 1541, doi:10.1175/JTECH-D-11-00208.1, URL https://journals.ametsoc.org/view/journals/atot/29/10/jtech-d-11-00208_1.xml.

Lance, S., C. A. Brock, D. Rogers, and J. A. Gordon, 2010: Water droplet calibration of the cloud droplet probe (cdp) and in-flight performance in liquid, ice and mixed-phase clouds during arcpac. *Atmospheric Measurement Techniques*, **3 (6)**, 1683–1706, doi:10.5194/amt-3-1683-2010, URL https://amt.copernicus.org/articles/3/1683/2010/.

Liljegren, J., 2004: Improved retrievals of temperature and water vapor profiles with a twelve-channel radiometer. *Bulletin of the American Meteorological Society*.

Maahn, M., D. D. Turner, U. Löhnert, D. J. Posselt, K. Ebell, G. G. Mace, and J. M. Comstock, 2020: Optimal estimation retrievals and their uncertainties: What every atmospheric scientist should know. *Bull. Am. Meteor. Soc.*, **101 (9)**, E1512 – E1523, doi:10.1175/BAMS-D-19-0027.1.

Mages, Z., P. Kollias, Z. Zhu, and E. P. Luke, 2023: Surface-based observations of cold-air outbreak clouds during the comble field campaign. *Atmos. Chem. Phys.*, **23**, 3561–3574, doi:10.5194/acp-23-3561-2023.

Mason, S. L., C. J. Chiu, R. J. Hogan, D. Moisseev, and S. Kneifel, 2018: Retrievals of riming and snow density from vertically pointing doppler radars. *Journal of Geophysical Research: Atmospheres*, **123 (24)**, 13,807–13,834, doi:https://doi.org/10.1029/2018JD028603, URL https://agupubs.onlinelibrary.wiley.com/doi/abs/10.1029/2018JD028603.

Mason, S. L., R. J. Hogan, C. D. Westbrook, S. Kneifel, D. Moisseev, and L. von Terzi, 2019: The importance of particle size distribution and internal structure for triple-frequency radar retrievals of the morphology of snow. *Atmospheric Measurement Techniques*, **12 (9)**, 4993–5018, doi:10.5194/amt-12-4993-2019, URL https://amt.copernicus.org/articles/12/4993/2019/.

McCluskey, C. S., and Coauthors, 2023: Simulating southern ocean aerosol and ice nucleating particles in the community earth system model version 2. *J. Geophysical Res.*, **128 (8)**, e2022JD036 955, doi:https://doi.org/10.1029/2022JD036955, e2022JD036955 2022JD036955.

McGrath, A., and T. Hewison, 2001: Measuring the accuracy of marss—an airborne microwave radiometer. *J. Atmos. Ocean. Tech.*, **18 (12)**, 2003 – 2012, doi:10.1175/1520-0426(2001)018⟨2003:MTAOMA⟩2.0.CO;2.

Mech, M., M. Maahn, S. Kneifel, D. Ori, E. Orlandi, P. Kollias, V. Schemann, and S. Crewell, 2020: Pamtra 1.0: the passive and active microwave radiative transfer tool for simulating radiometer and radar measurements of the cloudy atmosphere. *Geoscientific Model Development*, **13 (9)**, 4229–4251, doi:10.5194/gmd-13-4229-2020, URL https://gmd.copernicus.org/articles/13/4229/2020/.

Miles, N. L., J. Verlinde, and E. E. Clothiaux, 2000: Cloud droplet size distributions in low-level stratiform clouds. *Journal of the Atmospheric Sciences*, **57 (2)**, 295 – 311, doi:10.1175/1520-0469(2000)057⟨0295:CDSDIL⟩2.0.CO;2, URL https://journals.ametsoc.org/view/journals/atsc/57/2/1520-0469_2000_057_0295_cdsdil_2.0.co_2.xml.

Morrison, H., G. de Boer, G. Feingold, J. Harrington, M. D. Shupe, and K. Sulia, 2012: Resilience of persistent arctic mixed-phase clouds. *Nature Geoscience*, **1**, 11–17, doi:10.1038/ngeo1332.

Olson, J. B., J. S. Kenyon, W. Angevine, J. M. Brown, M. Pagowski, and K. Sušelj, 2019: A description of the MYNN-EDMF scheme and the coupling to other components in WRF-ARW. doi:10.25923/n9wm-be49.

Pazmany, A. L., 2007: A compact 183-ghz radiometer for water vapor and liquid water sensing. *IEEE Trans. Geosci. Rem. Sens.*, **45 (7)**, 2202–2206, doi:10.1109/TGRS.2006.888104.

Reynolds, R. W., T. M. Smith, C. Liu, D. B. Chelton, K. S. Casey, and M. G. Schlax, 2007: Daily high-resolution-blended analyses for sea surface temperature. *Journal of Climate*, **20 (22)**, 5473 – 5496, doi:10.1175/2007JCLI1824.1, URL https://journals.ametsoc.org/view/journals/clim/20/22/2007jcli1824.1.xml.

Rosenkranz, P. W., 1998: Water vapor microwave continuum absorption: A comparison of measurements and models. *Radio Science*, **33 (4)**, 919–928, doi:https://doi.org/10.1029/98RS01182, URL https://agupubs.onlinelibrary.wiley.com/doi/abs/10.1029/98RS01182.

Seethala, C., and Coauthors, 2024: Microphysical evolution in mixed-phase mid-latitude marine cold-air outbreaks. *J. Atmos. Sci.*, **81**, doi:10.1175/JAS-D-23-0203.

Sieron, S., F. Zhang, E. E. Clothiaux, and L. Yinghui, 2017: Coupling wrf microphysics parameterizations to community radiative transfer model simulations of microwave frequencies, towards data assimilation for tcs, pSU-UMD DA Workshop.

Skamarock, W. C., and J. B. Klemp, 2008: A time-split nonhydrostatic atmospheric model for weather research and forecasting applications. *J. Comput. Phys.*, **227**, 3465–3485.

Skamarock, W. C., and Coauthors, 2019: A description of the Advanced Research WRF version 4. NCAR Tech. Note NCAR/TN-556+STR.

Thompson, G., and T. Eidhammer, 2014: A study of aerosol impacts on clouds and precipitation development in a large winter cyclone. *J. Atmos. Sci.*, **71**, 3636–901.

Turner, D. D., S. A. Clough, J. C. Liljegren, E. E. Clothiaux, K. E. Cady-Pereira, and K. L. Gaustad, 2007: Retrieving liquid wat0er path and precipitable water vapor from the atmospheric radiation measurement (arm) microwave radiometers. *IEEE Transactions on Geoscience and Remote Sensing*, **45 (11)**, 3680–3690, doi:10.1109/TGRS.2007.903703.

Ulaby, F., R. Moore, and A. Fung, 1986: *Microwave Remote Sens.: Active and Passive. Vol. III. From theory to applications*. Artech House Publishers, doi:10.1017/S0016756800015831.

University of Wyoming - Flight Center, 1995: University of wyoming cloud radar (wcr). doi:10.15786/M2237S.

University of Wyoming - Flight Center, 2007: University of wyoming cloud lidar (wcl). doi:10.15786/M25W9D.

Walbröl, A., H. J. Griesche, M. Mech, S. Crewell, and K. Ebell, 2024: Combining low and high frequency microwave radiometer measurements from the mosaic expedition for enhanced water vapour products. doi:10.5194/egusphere-2024-1301.

Walbröl, A., and Coauthors, 2022: Atmospheric temperature, water vapour and liquid water path from two microwave radiometers during MOSAiC. *Sci. Data*, **9**, doi:10.1038/s41597-022-01504-1, 534.

Wang, Y., B. Geerts, and Y. Chen, 2016: Vertical structure of boundary layer convection during cold-air outbreaks at barrow, alaska. *J. Geophysical Research: Atmospheres*, **121 (1)**, 399–412, doi:https://doi.org/10.1002/2015JD023506, URL https://agupubs.onlinelibrary.wiley.com/doi/abs/10.1002/2015JD023506.

Wang, Z., and Coauthors, 2012: Single aircraft integration of remote sensing and in situ sampling for the study of cloud microphysics and dynamics. *Bull. Am. Meteor. Soc.*, **93 (5)**, 653 – 668, doi:10.1175/BAMS-D-11-00044.1, URL https://journals.ametsoc.org/view/journals/bams/93/5/bams-d-11-00044.1.xml.

Westwater, E., Y. Han, M. D. Shupe, and S. Y. Matrosov, 2001: Analysis of integrated cloud liquid and precipitable water vapor retrievals from microwave radiometers during the surface heat budget of the arctic ocean project. *J. Geophys. Res.*, **106**, 32 019–32 030.

Zuidema, P., and R. Joyce, 2008: Water vapor, cloud liquid water paths, and rain rates over the northern high latitude open seas. *J. Geophys. Res.*, **113**, doi:10.1029/2007JD009040, d05205.

Zuidema, P., A. Leon, D. andPazmany, and M. Cadeddu, 2012: Aircraft millimeter-wave passive sensing of cloud liquid water and water vapor during VOCALS-REx. *Atmos. Chem. Phys.*, **12**, 55–369, doi:10.5194/acp-12-355-2012.

Zuidema, P., E. R. Westwater, C. Fairall, and D. Hazen, 2005a: Ship-based liquid water path estimates in marine stratocumulus. *J. Geophys. Res.*, **110**, doi:10.1029/2005JD005833, d20206.

Zuidema, P., and Coauthors, 2005b: An arctic springtime mixed-phase cloudy boundary layer observed during SHEBA. *J. Atmos. Sci.*, **62**, 160–176.